OPTIMAL DESIGN AND SIMULATION-BASED VALIDATION OF A TOBACCO PLANTER BASED ON MULTIPLE BIRD-BEAK CHARACTERISTIC CURVES /

基于多鸟喙特征曲线的烟草栽植器优化设计与仿真验证

Sheng DING[1], Ao SHAN[2], Chencan XIAO [3], Qing JIANG[1,2,*]

[1] School of Mechanical and Vehicle Engineering, Anhui Agricultural University, Hefei 230036 / China;

[2] Anhui Provincial Engineering Research Center of Intelligent Agricultural Machinery, Hefei 230036. / China

Tel: 13349292716; E-mail: jtao@ahau.edu.cn

DOI: https://doi.org/10.35633/inmateh-79-101

Keywords: *biomimetic tobacco planter; penetration resistance; soil adhesion; discrete element method; Box–Behnken design*

ABSTRACT

To address the high penetration resistance and severe soil adhesion of tobacco planting devices operating in wet, clayey soil, a biomimetic planting device was designed using a Gaussian multi-peak function and characteristic curves derived from multiple bird beaks. The peak parameters, including height, position, and width, were optimized using discrete element method (DEM) simulations and response surface methodology. The resulting biomimetic profile reduced penetration resistance and soil adhesion, thereby improving tobacco transplanting performance. The optimized prototype exhibited a penetration resistance of 18.7 N and an adhered soil mass of 14.98 g, representing reductions of 60.47% and 40.56%, respectively, compared with the conventional prototype.

摘要

为解决烟草栽植器在湿黏土壤中阻力大、粘附严重的问题，本文基于高斯多峰函数融合多种鸟喙特征曲线，研制了一款仿生栽植器。结合离散元 (DEM) 仿真，利用响应面法优化了波峰参数（高度、位置和宽度）。该仿生曲线可以有效降低了渗透阻力、改善了土壤附着力，并提升了烟草移栽性能。优化后样机穿透阻力为 18.7 N，黏附质量为 14.98 g，相比于传统样机，分别减少了 60.47% 和 40.56%。

INTRODUCTION

Mechanized tobacco transplanting is strongly influenced by the interaction between the planter and the soil environment. As the primary soil-engaging component, the planter repeatedly penetrates the soil and plastic mulch during transplanting operations. Under wet and cohesive clay conditions, this repeated penetration may generate considerable penetration resistance and severe soil adhesion on the planter surface (*Obour et al., 2019; Xu et al., 2024*). These problems not only increase operational resistance and accelerate the wear of soil-engaging components, but may also adversely affect transplanting quality by causing excessive mulch damage, irregular planting holes, and seedling displacement. Therefore, reducing penetration resistance and soil adhesion is essential for improving the operational performance and reliability of tobacco planting equipment.

Biomimetic design has been increasingly applied to agricultural soil-engaging components by transferring the functional geometric or surface characteristics of biological organisms to engineering structures. Existing biomimetic approaches can generally be divided into two categories: surface microstructure modification and macroscopic contour optimization. Surface-based biomimetic designs typically reproduce the non-smooth or low-adhesion characteristics of biological surfaces. *Tong et al.* investigated the geometric features and wettability of dung beetle cuticles and demonstrated their potential for reducing soil adhesion on tillage implements (*Tong et al., 2005*). *Chen et al.* developed a pangolin-inspired concave microstructure that disrupted the interfacial water film and reduced the jacking force by 18.7% (*Chen et al., 2020*). *El Salem et al* verified that convex bionic surface configurations can break the continuity of soil-tool interfacial water films, decrease the actual contact area between soil and metal matrix, and achieve favorable anti-adhesion performance within viscous wet clay environments (*El Salem et al., 2023*).

Sheng Ding, M.S. Stud. Eng; Ao Shan, M.S. Stud.Eng; Chencan Xiao, M.S. Stud. Eng; Qing Jiang, Prof. Ph.D. Eng.

Similar discontinuous surface structures have also shown potential for reducing tillage resistance and soil adhesion under wet and cohesive soil conditions (*Niu et al., 2022; Zhang et al., 2025*).

In contrast, macroscopic contour optimization focuses on extracting and reproducing characteristic geometries from biological digging, burrowing, or penetrating organs. *Liu et al.* combined the morphological characteristics of the oriental mole cricket foreleg with soil mechanics to improve the digging performance of a cassava harvester (*Liu et al., 2014*). *Li et al. (2026)* investigated the soil burrowing mechanism of earthworms and *Liu et al. (2023)* developed a biomimetic furrow opener based on the head contour of an earthworm, whereas *Wu et al. (2021)* established a biomimetic mathematical model for subsoiling components based on biological geometric characteristics. These studies demonstrated that biomimetic contour optimization can effectively modify soil–tool interaction and reduce soil-engaging resistance. More recently, composite biomimetic strategies have been explored by combining different biological characteristics. *Guan et al. (2022)* integrated biological morphology with hydrophobic surface modification, while *Liu et al. (2024)* combined earthworm- and pangolin-inspired characteristics to reduce soil contact and adhesion.

Despite these advances, most existing biomimetic soil-engaging components are still based on simplified representations of a single biological feature (*Lei et al., 2024; Li et al., 2016; Lin et al., 2025; Sun et al., 2020; Wang et al., 2025*). Such single-feature designs may not fully satisfy the simultaneous requirements of low penetration resistance and reduced soil adhesion under the repeated dynamic penetration conditions encountered during tobacco transplanting. In addition, a unified mathematical framework capable of integrating complementary geometric characteristics from multiple biological prototypes into a continuously adjustable and optimizable contour remains insufficiently developed. Therefore, a multi-source biomimetic design method is needed to systematically combine different morphological characteristics and quantitatively optimize the resulting planter geometry.

To address this limitation, this study proposes a Gaussian multi-peak biomimetic design method for tobacco planters by integrating the characteristic beak contours of four bird species: the Common Kingfisher, Common Quail, Water Rail, and Common Ostrich. These biological prototypes were selected because they exhibit distinctly different beak geometries, including slender, short and robust, decurved, and broad profiles. The extracted contours were represented using a unified Gaussian multi-peak function, which enabled continuous and quantitative adjustment of peak height, peak position, and peak width. A Plackett–Burman screening design and a Box–Behnken response surface methodology were combined with discrete element method (DEM) simulations to identify the key geometric parameters and optimize the planter with respect to penetration resistance and soil adhesion. Furthermore, soil-particle velocity fields and disturbance characteristics were analyzed to investigate the mechanisms by which the optimized multi-peak contour promotes lateral soil diversion, tangential particle motion, and reduction of the frontal compression zone. The results provide a theoretical and methodological basis for designing tobacco planting components with reduced penetration resistance and improved anti-adhesion performance.

MATERIALS AND METHODS

Bionic Design

To address the high penetration resistance and severe soil adhesion encountered by tobacco planters during high-speed and repeated penetration into wet and cohesive soil, four bird species with distinctly different beak morphologies were selected as biological prototypes: the Common Kingfisher (S1), Common Quail (S2), Water Rail (S3), and Common Ostrich (S4), as shown in Fig. 1. The Common Kingfisher has a slender and approximately conical beak with a relatively small tip angle and a smooth longitudinal profile *(Crandell et al., 2019*). The Common Quail has a shorter and more robust beak with concentrated curvature variation near the anterior region (*Zhang X.Y. et al., 2021*). The Water Rail has a slender and moderately decurved beak *(Bouzid et al., 2023*), whereas the Common Ostrich has a broader profile with a comparatively large obtuse tip angle (*Zhang R. et al., 2021*). These four beak geometries represent different morphological characteristics and provide a diverse geometric basis for multi-source biomimetic contour integration and subsequent parametric optimization.

The bird images used for contour extraction were obtained from publicly available online sources, with an approximate original resolution of 1200 × 800 pixels. Original camera and lens metadata were not available because the images were obtained from public online sources. Therefore, image selection was controlled by lateral-view orientation, clear beak boundaries, and the absence of obvious perspective distortion. To ensure reliable contour extraction, only images showing the beak approximately in lateral view, with clear and unobstructed boundaries and no obvious perspective distortion, were selected.

Because this study focused on normalized geometric profiles rather than absolute biological dimensions, all extracted coordinates were normalized to a dimensionless scale before curve fitting to minimize the effects of differences in image scale.

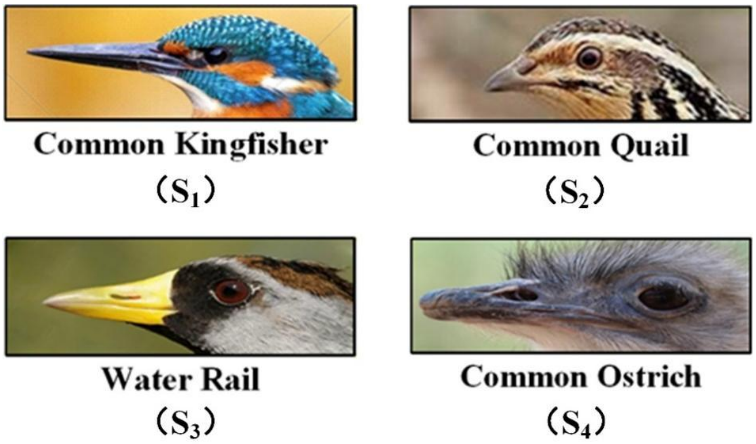

Fig. 1 - Images of the bionic prototypes for the selected bird beaks

The beak-contour extraction procedure is illustrated in Fig. 2. Image processing was performed using MATLAB R2023b (MathWorks, Natick, MA, USA). Grayscale conversion, Otsu thresholding, Canny edge detection, and contour-coordinate extraction were successively conducted. The extracted upper-beak contour was then resampled into 100 equally spaced points along the arc length for subsequent dimensionless normalization and Gaussian multi-peak fitting. The extracted contours were then corrected by affine transformation so that the beak tip coincided with the coordinate origin and the principal longitudinal axis was aligned with the horizontal axis. The normalization equations were:

$$x^* = \frac{x - x_{min}}{x_{max} - x_{\min}}, y^* = \frac{y - y_{\min}}{y_{max} - y_{\min}} \tag{1}$$

x and y are the original contour coordinates; x_{min} and x_{max} are the minimum and maximum values of the x-coordinates, respectively; y_{min} and y_{max} are the minimum and maximum values of the y-coordinates, respectively; and x^* and y^* are the normalized dimensionless coordinates.

To achieve a unified parametric representation of the different bird-beak contours, a Gaussian multi-peak function was used to fit the normalized contour data:

$$f(x) = \sum_{i=1}^{n} a_i e^{-\left(\frac{x-b_i}{c_i}\right)^2} \tag{2}$$

where: $f(x)$ is the fitted value at position x; n is the total number of Gaussian terms; i denotes the current Gaussian component; and a_i, b_i, and c_i represent the peak height, peak position, and peak width of the i-th Gaussian component, respectively.

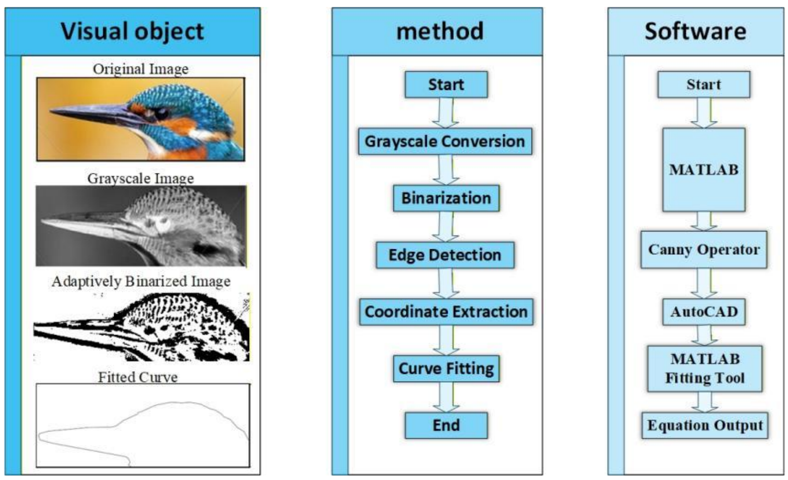

Fig. 2 - Flowchart of image processing and contour extraction

The Gaussian multi-peak function was selected because it can flexibly describe complex biological contours using a limited number of independent parameters, while each parameter has an explicit geometric meaning that allows complex beak morphologies to be converted into continuous, adjustable, and quantifiable engineering design variables. In addition, this parametric representation facilitates subsequent Plackett–Burman screening and Box–Behnken response-surface optimization, thereby reducing the dimensionality of the optimization problem and improving computational efficiency.

The goodness of fit was evaluated using both the coefficient of determination (R^2) and the root mean square error ($RMSE$), calculated as:

$$RMSE = \sqrt{\frac{1}{N}\sum_{j=1}^{N}\left(y_j - \hat{y}_j\right)^2} \tag{3}$$

where:

N is the number of sampled contour points; y_j is the actual normalized contour coordinate of the j-th sampling point; and $\hat{y}_j$ is the corresponding fitted value. The Gaussian multi-peak parameters and fitting evaluation indices of the four bird-beak contours are summarized in Table 1. The R^2 values ranged from 0.9506 to 0.9908, while the $RMSE$ values ranged from 0.0192 to 0.0445, indicating that the Gaussian multi-peak function adequately represented the principal geometric characteristics of the four bird-beak contours.

Table 1

Bionic planter curve parameters

Coefficient	Beak ID			
	S_1	S_2	S_3	S_4
a_1	0.9851	0.9894	0.9722	0.9486
b_1	0.9078	0.9900	0.9272	0.8856
c_1	0.4116	0.3577	0.3673	0.4189
a_2	0.30348	0.3574	0.4918	0.3559
b_2	0.2880	0.3532	0.3462	0.2378
c_2	0.1851	0.1847	0.1861	0.1322
R^2	0.9854	0.9908	0.9727	0.9506
RMSE	0.0241	0.0192	0.0336	0.0445

Structural Design

The planter is the main soil-engaging component in tobacco transplanting and adopts a symmetrical double-valve structure to perform hole formation and seedling release simultaneously. The overall structure is shown in Fig. 3. Its motion is controlled by a linkage mechanism consisting of a pull rod, a rotating shaft, and two movable plates. During the downward stroke, the external driving mechanism actuates the pull rod, causing the two movable plates to rotate outward around the shaft and open the duckbill at the predetermined depth. During the return stroke, the assembly returns to its initial position under the combined effects of the return spring and gravity, preparing for the next working cycle.

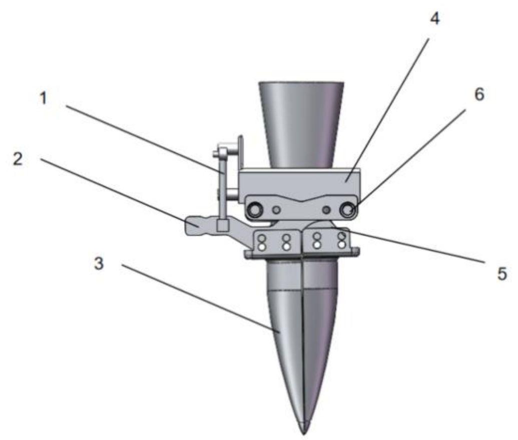

Fig. 3 - Overall structure diagram of the bionic planter

(1) Pull rod (2) Movable plate I (3) Planter (4) Planter bracket (5) Movable plate II; (6) Rotating shaft

The three-dimensional model of the planter was developed using SolidWorks 2024. The main body was designed using 304 stainless steel and was intended for fabrication by metal additive manufacturing. The planter geometry was exported from SolidWorks 2024 as a binary STL surface model and imported into EDEM. A custom STL export resolution was used, with the unit set to millimeters, a surface deviation tolerance of 0.154 mm, and an angular tolerance of 10°. The overall dimensions of the planter were 110 mm × 250 mm × 100 mm, with a wall thickness of 2 mm. The calculated mass based on the CAD model was 0.676 kg, and a nominal dimensional tolerance of ±0.5 mm was specified in the design.

The internal cavity of the planter was dimensioned to ensure compatibility with seedlings cultivated in standard 128-cell plug trays. The seedling plug had an upper diameter of 30 mm, a lower diameter of 10 mm, and a height of 40 mm, as shown in Fig. 4(a). For the subsequent discrete element simulation, the complex morphology of the actual tobacco seedling was simplified and represented by a regular geometric model to establish the internal geometric boundary of the planter, as shown in Fig. 4(b). This simplification reduced the computational complexity associated with complex leaves, stems, and irregular plug geometry. Since the present study mainly focused on the interaction between the external planter surface and wet cohesive soil, particularly the maximum penetration resistance and soil adhesion mass, the detailed morphology of the actual seedling was not explicitly modeled. However, this simplification may neglect local contact and posture variations between the actual seedling and the inner wall of the planter. No separate sensitivity analysis was conducted for the simplified seedling geometry; therefore, its influence on simulation accuracy was not quantitatively assessed. The proposed design was intended to address two major constraints associated with the regional soil conditions: the strong interfacial adhesion of high-moisture clay, which causes severe soil adhesion and accumulation on the planter surface, and the high penetration resistance generated by compacted soil. Typical field soil conditions are shown in Fig. 5. Therefore, the integration of multiple bird-beak characteristic curves into the planter design is intended to reduce soil adhesion and penetration resistance.

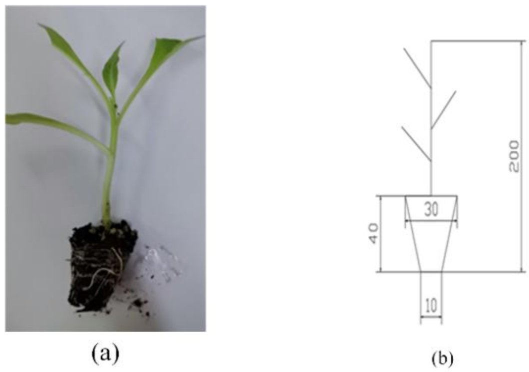

Fig. 4 - Morphological characteristics of the target tobacco seedling
(a) actual biological specimen; (b) simplified geometric model.

Fig. 5 - Field soil exhibiting high penetration resistance and strong adhesion

Experimental Design

To identify the main factors controlling the soil-engaging performance of the planter, the experimental design was conducted in two stages.

First, a Plackett–Burman (PB) screening design was used to evaluate the six morphological parameters (a_1, b_1, c_1, a_2, b_2, and c_2) and identify the factors influencing the maximum penetration resistance (Y_1) and soil adhesion mass (Y_2). These six parameters were derived from the two-term Gaussian multi-peak function, in which each Gaussian term was defined by three independent parameters corresponding to peak height, peak position, and peak width. Therefore, the six parameters jointly characterized the complete geometry of the biomimetic contour.

The maximum penetration resistance (Y_1) was selected to characterize the mechanical resistance encountered by the planter during soil penetration and was closely related to operational energy consumption. The soil adhesion mass (Y_2) was used to quantify the amount of wet cohesive soil retained on the planter surface, which may affect the continuous operating performance of the planter.

The factor levels, configured as high (+1) and low (-1) levels, were determined according to the geometric parameter ranges extracted from the four bird-beak prototypes, thereby ensuring that the investigated design space had a clear biological basis. The factor levels are given in Table 2.

Second, based on the PB screening results, the three factors exerting the greatest influence on soil-engaging performance were selected for further analysis of interaction effects and parameter optimization using a three-factor, three-level Box–Behnken design (BBD), with coded levels of -1, 0, and +1. For three factors, the standard BBD consisted of 12 factorial combination points and five center-point runs, resulting in a total of 17 experimental runs. All design points were simulated under identical numerical settings. The five center-point runs were used to estimate the pure error and evaluate the numerical repeatability of the response surface model.

Table 2

Factors and levels of the Plackett-Burman experimental design

Factor	Low level (-1)	High level (+1)
a_1	0.9486	0.9894
b_1	0.8856	0.9900
c_1	0.3577	0.4189
a_2	0.3034	0.4918
b_2	0.2378	0.3532
c_2	0.1322	0.1861

The interaction dynamics of these experimental runs were simulated using EDEM 2024 software. The Hertz-Mindlin with JKR cohesion contact model was used to represent the cohesive behavior and interfacial adhesion characteristics of wet cohesive clay.

The soil particles were represented by three types of particle aggregates, namely single-sphere, double-sphere, and triple-sphere particles, with particle sizes ranging from 1.5 to 3.0 mm. The proportions of single-sphere, double-sphere, and triple-sphere particles were 60%, 25%, and 15%, respectively, and a total of 100,000 particles were generated in the soil bin.

The particles were generated, allowed to settle under gravity, and then statically compacted using a flat compaction plate to reproduce natural field soil conditions. The penetration simulation was started after the compacted soil bed became stable, as indicated by a low and nearly constant total kinetic energy and no obvious change in bed height. The planter material was modeled as 304 stainless steel.

The setup of the simulation model is shown in Fig. 6, and the complete list of the intrinsic and contact mechanics parameters is given in Table 3.

The Euler integration scheme was adopted, with a fixed time step of 6.47855×10^{-5} s, corresponding to 20% of the Rayleigh time step. The total simulation time was 2.5 s, and simulation data were saved at intervals of 0.001 s. The simulations were performed using the CPU solver with 12 CPU cores. All simulations were conducted on a workstation equipped with a 12th Gen Intel Core i5-12400F processor and 32 GB of RAM.

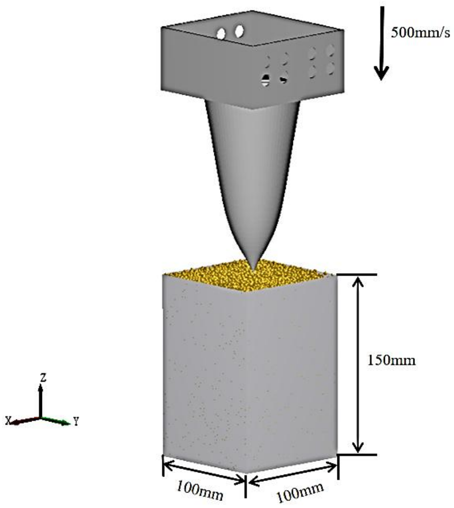

Fig. 6 - Discrete Element Method (DEM) simulation model

Table 3

Intrinsic and contact parameters of the discrete element simulation model

Item	Parameter	Value
Soil properties	Soil density / kg·m⁻³	2760
	Soil Poisson's ratio	0.35
	Soil shear modulus / MPa	1.5
Stainless-steel properties	Stainless steel density / kg·m⁻³	7850
	Stainless steel Poisson's ratio	0.3
	Stainless steel shear modulus / MPa	7x10^4
Soil-soil contact parameters	Soil-soil JKR surface energy / J·m⁻²	4.982
	Coefficient of restitution	0.411
	Coefficient of static friction	0.78
	Coefficient of rolling friction	0.148
Soil–stainless-steel contact parameters	Soil-stainless steel JKR surface energy / J·m⁻²	2.027
	Coefficient of restitution	0.599
	Coefficient of static friction	0.711
	Coefficient of rolling friction	0.015

Statistical analysis and response surface modeling were performed using Design-Expert 13.0.5.0 software (Stat-Ease Inc., Minneapolis, MN, USA), with the significance level set at α = 0.05. The adequacy of the regression models was evaluated using ANOVA, R^2, adjusted R^2, predicted R^2, lack-of-fit test, and adequate precision. Residual diagnostics were conducted using normal probability plots of residuals, residuals versus predicted values, and Cook's distance. The predictive performance of the models was further evaluated by comparing the predicted responses with the corresponding results from independent DEM numerical verification.

RESULTS

Analysis of Key Parameter Screening Tests

The Plackett–Burman screening results are shown in Table 4. The maximum penetration resistance (Y_1) ranged from 25.21 N to 34.12 N, and the soil adhesion mass (Y_2) ranged from 12.40 g to 21.80 g, indicating that the Gaussian contour parameters had an obvious influence on the soil-engaging performance of the planter.

To quantify the relative influence of each parameter, the main effects and percentage contributions were calculated from the screening results. For penetration resistance, a_2 showed the largest positive effect, with a contribution of 54.83%, followed by c_2 and b_2, with contributions of 27.38% and 13.50%, respectively. This indicates that the front-end peak height was the dominant factor increasing penetration resistance, while a larger peak width helped reduce resistance by producing a smoother surface transition.

For soil adhesion mass, c_2 was the dominant factor, with a contribution of 72.00%, followed by a_2, with a contribution of 12.79%. This result indicates that the peak width mainly controlled soil adhesion by affecting the smoothness of the planter surface and the sliding behavior of wet cohesive soil. The effects of the back-end parameters a_1, b_1, and c_1 were relatively small for both response variables.

As shown in the standardized Pareto charts in Fig. 7, the front-end Gaussian parameters a_2, b_2, and c_2 had greater effects on the two response variables than the back-end parameters. Therefore, a_2, b_2, and c_2 were selected as the key design variables for the subsequent Box–Behnken response surface optimization, while a_1, b_1, and c_1 were fixed in the following optimization process.

Table 4

Plackett-Burman experimental design scheme and response results

Test No.	Factor						Penetration Resistance [N]	Soil adhesion mass [g]
	a_1	b_1	c_1	a_2	b_2	c_2		
1	+1	+1	-1	+1	+1	+1	29.86	15.6
2	-1	+1	+1	-1	+1	+1	25.21	12.4
3	+1	-1	+1	+1	-1	+1	28.14	13.8
4	-1	+1	-1	+1	+1	-1	33.85	21.5
5	-1	-1	+1	-1	+1	+1	25.68	12.9
6	-1	-1	-1	+1	-1	+1	27.92	13.5
7	+1	-1	-1	-1	+1	-1	29.15	18.1
8	+1	+1	-1	-1	-1	+1	26.54	16.4
9	+1	+1	+1	-1	-1	-1	26.88	16.8
10	-1	+1	+1	+1	-1	-1	30.06	18.3
11	+1	-1	+1	+1	+1	-1	34.12	21.8
12	-1	-1	-1	-1	-1	-1	26.35	16.1

Table 5

Main effects and percentage contributions of the Plackett–Burman screening results

Factor	Effect on Y_1 [N]	Contribution to Y_1 [%]	Effect on Y_2 [g]	Contribution to Y_2 [%]
a_1	0.94	2.97	1.30	5.59
b_1	0.17	0.10	0.80	2.12
c_1	-0.60	1.21	-0.87	2.48
a_2	4.02	54.83	1.97	12.79
b_2	2.00	13.50	1.23	5.03
c_2	-2.84	27.38	-4.67	72.00

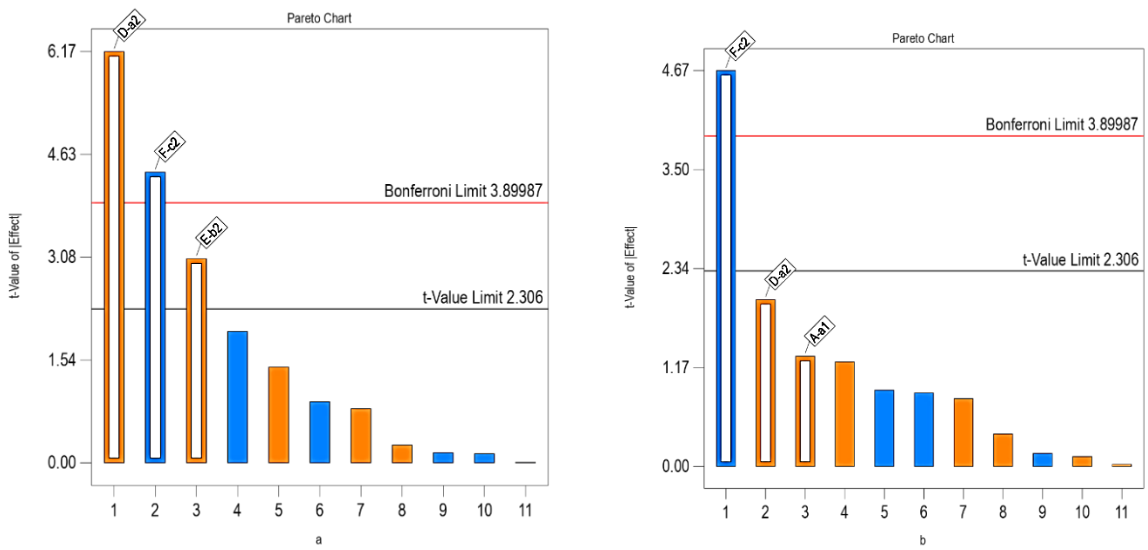

Fig. 7 - Standardized Pareto charts of main effects

(a) penetration resistance; (b) soil adhesion mass.

Box–Behnken Design and Response Surface Model Fitting

According to the Plackett–Burman screening results, the peak height (a_2), peak position (b_2), and peak width (c_2) were selected as the main biomimetic parameters affecting the soil-engaging performance of the planter. A three-factor, three-level Box–Behnken design was used to analyze the effects of these parameters and their interactions on the maximum penetration resistance (Y_1) and soil adhesion mass (Y_2). The coded levels of the three factors are listed in Table 6, and the design matrix and corresponding EDEM simulation results are shown in Table 7.

Table 6

Factors and coded levels of Box-Behnken design

Coded level	Factor		
	a_2	b_2	c_2
1	0.4918	0.3532	0.1861
0	0.3983	0.2955	0.1592
-1	0.3048	0.2378	0.1322

Table 7

Response surface experimental design and EDEM simulation results

Standard Order	Factor			Penetration Resistance [N]	soil adhesion mass [g]
	a_2	b_2	c_2		
1	-1	-1	0	21.9	14.21
2	1	-1	0	35.11	21.24
3	-1	1	0	18.8	12.56
4	1	1	0	32.46	20.54
5	-1	0	-1	20.54	15.56
6	1	0	-1	33.85	20.35
7	-1	0	1	18.6	12.48
8	1	0	1	28.34	18.43
9	0	-1	-1	22.59	17.36
10	0	1	-1	19.46	18.96
11	0	-1	1	20.85	15.12
12	0	1	1	17.65	15.86
13	0	0	0	24.15	16.52
14	0	0	0	23.98	16.41
15	0	0	0	24.32	16.65
16	0	0	0	24.05	16.38
17	0	0	0	24.21	16.55

As shown in Table 7, the maximum penetration resistance ranged from 17.65 N to 35.11 N, and the soil adhesion mass ranged from 12.48 g to 21.24 g. The five center-point runs showed small variations. The penetration resistance values of the center points were 24.15, 23.98, 24.32, 24.05, and 24.21 N, with a mean value of 24.14 N and a standard deviation of 0.13 N. The corresponding soil adhesion mass were 16.52, 16.41, 16.65, 16.38, and 16.55 g, with a mean value of 16.50 g and a standard deviation of 0.11 g. These results indicate that the DEM simulation had good numerical repeatability under the same simulation conditions.

The ANOVA results of the fitted models are shown in Table 8. The quadratic model for penetration resistance was extremely significant (p < 0.0001), with R^2, adjusted R^2, and predicted R^2 values of 0.9916, 0.9808, and 0.8676, respectively. The adequate precision was 30.7602, which was much higher than the recommended threshold of 4. For penetration resistance, the linear terms a_2, b_2 and c_2 were all extremely significant (p < 0.01). The interaction term a_2c_2 was significant (p = 0.0467), while a_2b_2 and b_2c_2 were not significant. The quadratic terms a_2^2, b_2^2, and c_2^2 were also significant, indicating a nonlinear relationship between the front-end contour parameters and penetration resistance.

The linear model for soil adhesion mass was also extremely significant (p < 0.0001), with R^2, adjusted R^2, and predicted R^2 values of 0.9343, 0.9192, and 0.8665, respectively. The adequate precision was 25.7831, indicating that the model had sufficient signal for response prediction within the selected design space.

For soil adhesion mass, a_2 and c_2 were extremely significant (p < 0.01), whereas b_2 was not significant (p = 0.9962). This result indicates that soil adhesion was mainly affected by peak height and peak width rather than peak position.

Although the lack-of-fit terms of both models were significant (p < 0.05), this may be attributed to the nonlinear friction, collision, cohesion, and adhesion behavior between wet clay particles and the biomimetic planter surface in the DEM simulation. Considering the high model significance, high R^2 values, and adequate precision values, the fitted models were considered acceptable for empirical optimization within the selected design space. However, they should not be interpreted as universal prediction models outside the investigated factor ranges.

The PRESS values of the penetration resistance model and soil adhesion mass model were 60.39 and 13.76, respectively. These values, together with the predicted R^2 values, were used to evaluate the predictive performance of the fitted regression models within the selected design space.

Table 8

Analysis of variance (ANOVA) for the regression models of penetration resistance and soil adhesion

Source	Penetration resistance (Y_1)			Soil adhesion (Y_2)		
	df	F-value	p-value	df	F-value	p-value
Model	9	91.62	<0.0001**	3	61.64	<0.0001**
A-a_2	1	568.07	<0.0001**	1	159.25	<0.0001**
B-b_2	1	33.27	0.0007**	1	0	0.9962ns
C-c_2	1	27.58	0.0012**	1	25.68	0.0002**
AB	1	0.0923	0.7701ns	-	-	-
AC	1	5.81	0.0467*	-	-	-
BC	1	0.0022	0.9636ns	-	-	-
A^2	1	126.59	<0.0001**	-	-	-
B^2	1	9.89	0.0163*	-	-	-
C^2	1	63.24	<0.0001**	-	-	-
Lack of Fit	3	70.67	0.0006*	9	62.36	0.0006*
R^2	0.9916			0.9343		
Adjusted R^2	0.9808			0.9192		
Predicted R^2	0.8676			0.8665		
Adeq Precision	30.7602			25.7831		
PRESS	60.39			13.76		

*Note: ** indicates extremely significant (p < 0.01); * indicates significant (p < 0.05); ns indicates not significant (p > 0.05); "-" indicates that the model does not include this term.*

Model Diagnostic Analysis

The diagnostic plots of the fitted response surface models are shown in Fig.8. For both response models, most residual points were approximately distributed along the reference line in the normal probability plots, indicating that no serious deviation from normality was observed. In the residuals versus predicted values plots, the residuals were generally distributed around zero, suggesting that the fitted models could describe the response trends within the selected design space.

The Cook's distance plots showed that several design points had relatively high influence on the fitted models. This may be related to the nonlinear friction, collision, cohesion, and adhesion behavior of wet cohesive soil particles during DEM simulation. These points were not removed because they corresponded to valid parameter combinations in the Box–Behnken design. Therefore, the regression models were used as empirical optimization models within the investigated factor ranges, and the optimized results were further evaluated by independent DEM numerical verification.

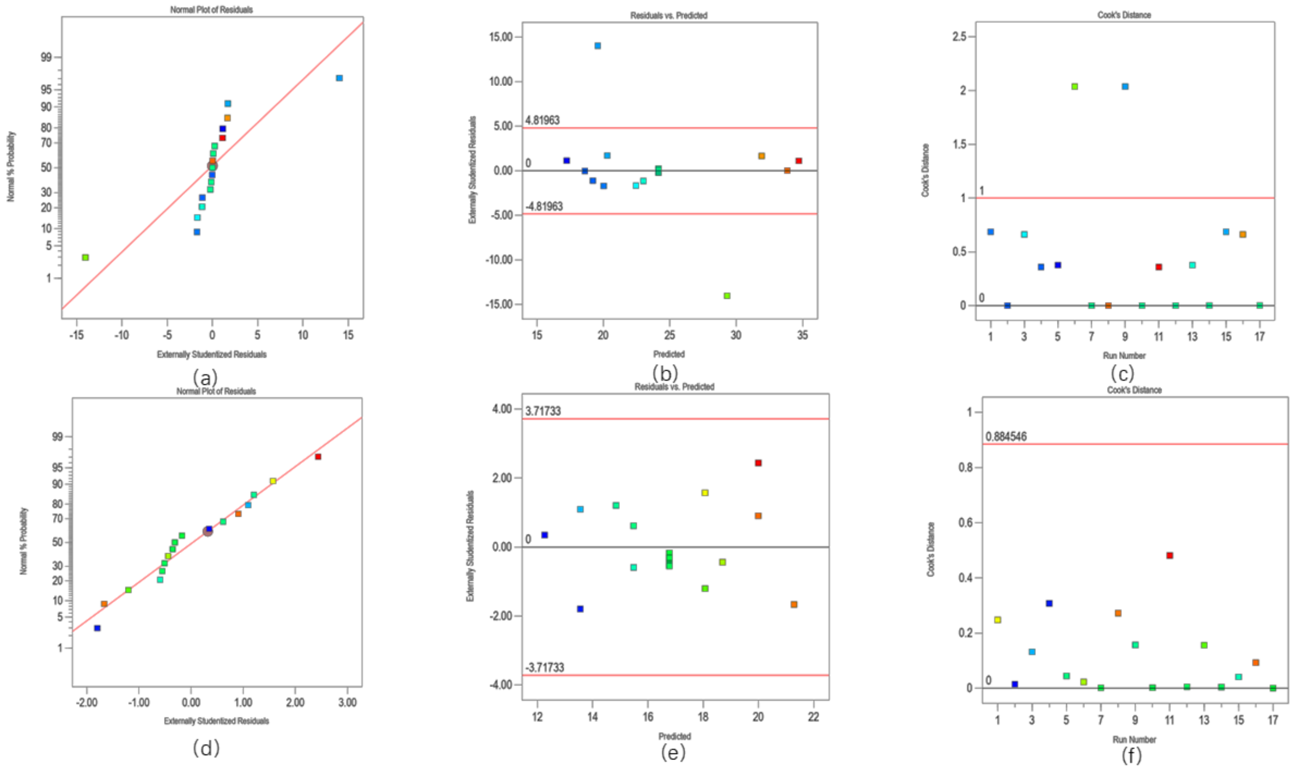

Fig. 8 - Diagnostic plots of the fitted response surface models

(a) normal probability plot of residuals for Y_1; (b) residuals versus predicted values for Y_1;
(c) Cook's distance for Y_1; (d) normal probability plot of residuals for Y_2;
(e) residuals versus predicted values for Y_2; (f) Cook's distance for Y_2.

According to the BBD analysis, the real factor regression equations of maximum penetration resistance (Y_1) and the soil adhesion mass (Y_2) for the peak height (a_2), peak position (b_2) and peak width (c_2) are as follows:

$$\mathrm{Y}_1 = -63.274 - 253.027a_2 + 168.751b_2 + 1351.039c_2 + 20.853a_2b_2 - 354.191a_2c_2 - 11.254b_2c_2 + 464.440{a_2}^2 - 340.838{b_2}^2 - 3951.177{c_2}^2 \tag{4}$$

$$Y_2 = 10.703 + 34.425a_2 - 0.022b_2 - 47.959c_2 \tag{5}$$

Response Surface Analysis

The response surface plots are shown in Fig. 9. For penetration resistance, the response surfaces of the a_2 b_2 and b_2 c_2 interactions were relatively smooth, which is consistent with the ANOVA results showing that these two interaction terms were not significant ($p > 0.05$). This indicates that changing the peak position (b_2) did not strongly alter the effect of peak height or peak width on penetration resistance.

In contrast, the interaction between a_2 and c_2 had a significant effect on penetration resistance ($p < 0.05$). When a_2 was high, the penetration resistance remained relatively high, because a larger front-end peak increased the frontal soil-breaking area and enhanced soil compression. When a_2 was low and c_2 was high, the penetration resistance decreased. This indicates that a lower peak height helped reduce frontal compression, while a larger peak width produced a smoother surface transition and promoted soil sliding along the planter surface.

For soil adhesion mass, the response surface showed an approximately linear trend. Soil adhesion increased with increasing a_2 and decreased with increasing c_2. This result indicates that the peak height and peak width mainly controlled soil adhesion by changing the local contact and sliding behavior between wet clay and the planter surface. Therefore, the protrusion height and surface smoothness should be jointly optimized to achieve both resistance reduction and adhesion reduction.

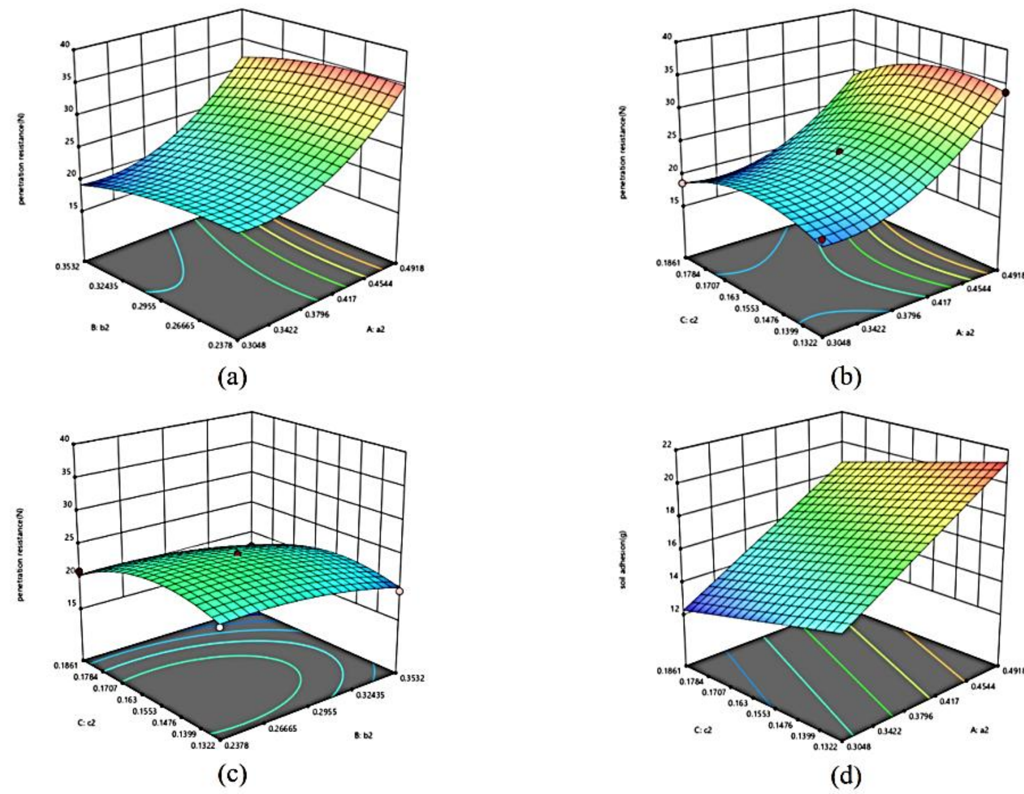

Fig. 9 - Response surface plots illustrating the interactive effects of biomimetic parameters

(a) a_2 and b_2 on penetration resistance (Y_1); (b) b_2 and c_2 on Y_1; (c) a_2 and c_2 on Y_1; (d) a_2 and c_2 on soil adhesion (Y_2)

Objective Function Establishment and Parameter Optimization

The objective is to minimize both the maximum penetration resistance (Y_1) and soil adhesion (Y_2) with the physical constraints of the planter's structure.

The optimization model is as follows:

$$\begin{cases} min\, Y_1 = f_1(a_2, b_2, c_2) \\ min\, Y_2 = f_2(a_2, b_2, c_2) \\ s.t. \\ 0.3048 \le a_2 \le 0.4918 \\ 0.2378 \le b_2 \le 0.3532 \\ 0.1322 \le c_2 \le 0.1861 \end{cases} \tag{6}$$

The desirability function method was used to integrate the two response variables into an overall desirability index (D) calculated as follows:

$$D = (d_1(Y_1) \times d_2(Y_2))^{\frac{1}{2}} \tag{7}$$

where: d_1 and d_2 are the individual desirability values for penetration resistance and soil adhesion.

The optimization objective was to minimize both the maximum penetration resistance (Y_1) and soil adhesion mass (Y_2) within the selected design space. The desirability function method in Design-Expert was used to integrate the two response variables into a comprehensive desirability index. The optimized parameter combination was a_2 = 0.30, b_2 = 0.35, and c_2 = 0.19, with an overall desirability value of 0.893. Under this condition, the predicted penetration resistance and soil adhesion mass were 16.14 N and 12.40 g, respectively.

Other optimization algorithms, such as genetic algorithms and particle swarm optimization, were also considered. However, the present optimization problem involved only three continuous design variables and two response objectives, and the fitted response surface models provided explicit regression equations within the selected design space. Therefore, the desirability function method was adopted because it could directly integrate penetration resistance and soil adhesion mass into a single interpretable optimization index. Population-based optimization algorithms may be considered in future work when more design variables, structural constraints, or experimental validation data are included.

Parameter Optimization and Numerical Verification

To evaluate the optimized parameter combination, the optimized planter model was reconstructed and an independent DEM simulation was conducted under the same numerical conditions. Since this study focused on numerical optimization, the verification was based on DEM simulation rather than laboratory or field experiments. Therefore, the verification results should be interpreted as numerical verification within the DEM framework. The soil particle velocity fields of the conventional prototype, the four single bird-beak biomimetic profiles (S_1–S_4), and the optimized multi-peak profile are shown in Fig. 10.

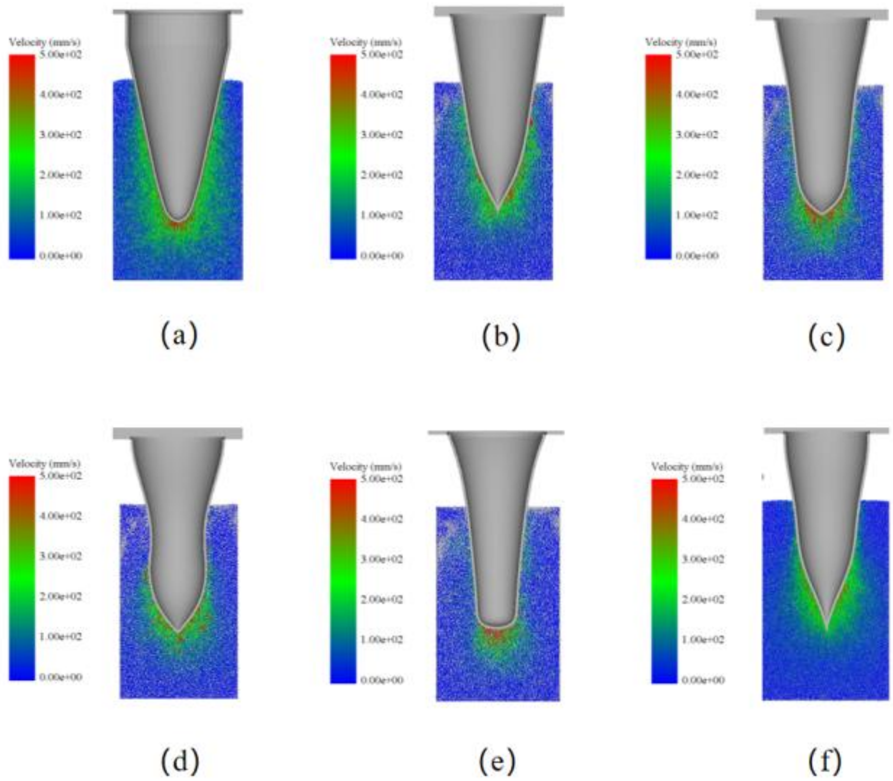

Fig. 10 - Comparison of soil particle velocity fields for different planter profiles
(a) Conventional (b-e) Bionic prototypes S_1-S_4 (f) Optimized multi-peak bionic profile

As shown in Fig. 10(a), the conventional planter produced a wide V-shaped high-velocity disturbance zone during soil penetration, indicating strong frontal compression and large-scale soil disturbance. In contrast, the optimized multi-peak biomimetic planter generated a narrower and more streamlined disturbance zone, and the soil particles tended to move along the planter surface, as shown in Fig. 10(f). This indicates that the dominant soil motion changed from frontal compression to tangential sliding, thereby reducing local soil compaction and weakening soil accumulation on the planter surface.

To quantitatively evaluate the resistance-reduction and anti-adhesion effects, the penetration resistance and soil adhesion mass were extracted for all planter profiles, as shown in Fig. 11. The maximum penetration resistance of the conventional prototype was 47.30 N, whereas that of the optimized biomimetic planter was 18.70 N, corresponding to a reduction of 60.47%. The soil adhesion mass decreased from 25.20 g for the conventional prototype to 14.98 g for the optimized planter, corresponding to a reduction of 40.56%.

As shown in Table 9, the predicted penetration resistance and soil adhesion mass were 16.14 N and 12.40 g, respectively, while the corresponding DEM verification values were 18.70 N and 14.98 g. The relative errors were 15.86% and 20.81%, respectively. Although the DEM verification values were higher than the predicted values, the optimized model showed a consistent reduction trend and was therefore acceptable for evaluating the optimization direction. Mechanistically, the optimized peak height and peak width produced a smoother transition of the planter surface, which reduced frontal soil compression and promoted tangential soil sliding. This change in soil motion reduced penetration resistance and weakened the retention of wet cohesive soil on the planter surface. Overall, the optimized multi-peak configuration achieved coupled reductions in penetration resistance and soil adhesion mass.

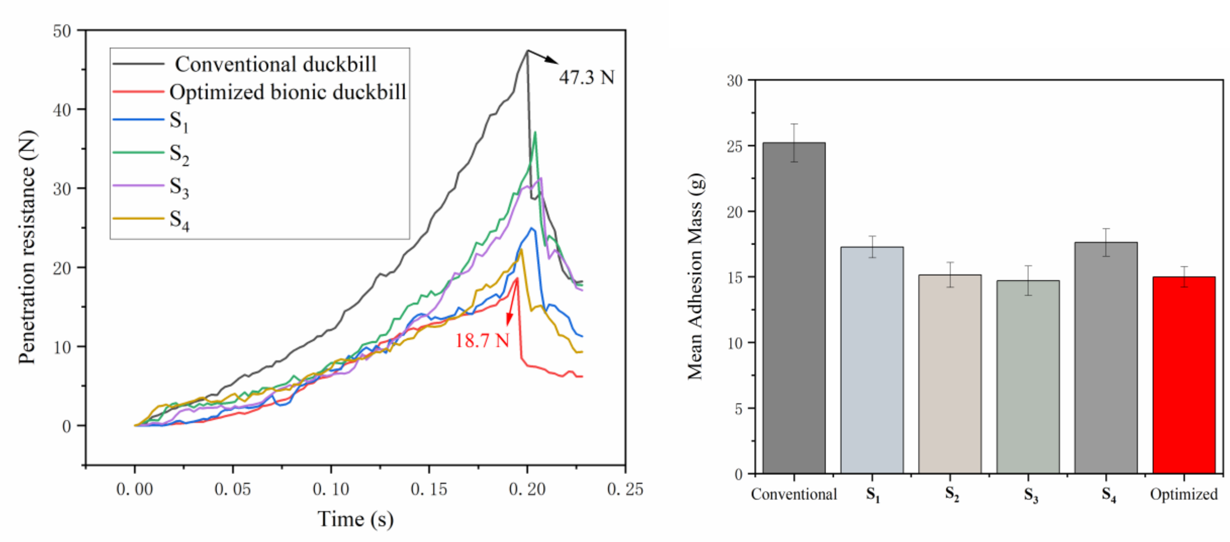

Fig. 11 - Soil-engaging performance of different planter profiles
(a) Penetration resistance curves (b) Mean adhesion mass

Table 9

Numerical verification results of the optimized parameter combination

Response	Predicted value	DEM verification value	Relative error [%]
Y_1 / [N]	16.14	18.70	15.86
Y_2 / [g]	12.40	14.98	20.81

CONCLUSIONS

In this study, a Gaussian multi-peak biomimetic tobacco planter was designed by integrating the characteristic beak contours of multiple bird species. DEM simulation, Plackett–Burman screening, Box–Behnken response surface optimization, and independent DEM numerical verification were used to evaluate the effects of the biomimetic contour parameters on penetration resistance and soil adhesion mass.

The Plackett–Burman screening results showed that the front-end Gaussian parameters a_2, b_2, and c_2 had greater effects on penetration resistance and soil adhesion mass than the back-end parameters. Therefore, a_2, b_2, and c_2 were selected as the key variables for response surface optimization. Based on the Box–Behnken design and desirability function method, the optimized parameter combination was obtained as a_2 = 0.30, b_2 = 0.35, and c_2 = 0.19. Under this condition, the predicted penetration resistance and soil adhesion mass were 16.14 N and 12.40 g, respectively. The independent DEM verification values were 18.70 N and 14.98 g, with relative errors of 15.86% and 20.81%, respectively.

Compared with the conventional planter, the optimized multi-peak biomimetic planter reduced the maximum penetration resistance from 47.30 N to 18.70 N and reduced the soil adhesion mass from 25.20 g to 14.98 g, corresponding to reductions of 60.47% and 40.56%, respectively. The optimized profile also showed better combined resistance-reduction and anti-adhesion performance than the single bird-beak biomimetic profiles.

The soil particle velocity field showed that the optimized multi-peak profile reduced the wide V-shaped frontal disturbance zone and promoted soil motion along the planter surface. This indicates that the dominant soil motion changed from frontal compression to tangential sliding, thereby reducing local soil compaction and weakening the retention of wet cohesive soil on the planter surface.

It should be noted that the verification in this study was based on independent DEM simulation rather than laboratory or field experiments. Therefore, the results should be interpreted as numerical verification within the selected design space. Future work will focus on prototype fabrication and experimental validation under actual tobacco transplanting conditions.

REFERENCES

[1] Bouzid A., Samraoui F., & Samraoui B. (2023). A survey of the distribution of the water rail Rallus aquaticus in Algeria and its first recorded breeding in the Algerian Sahara. *African journal of ecology*. https://doi.org/10.1111/aje.13119

[2] Chen D.H., Yang X., Dai T.D., Sun Y.H., & Chang Z.Y. (2020). Bionic Design to Reduce Jacking Force for Trenchless Installations in Clay Soil. *Journal of bionic engineering*, 17(4), 686–694. https://doi.org/10.1007/s42235-020-0066-8

[3] Crandell K.E., Howe R.O., & Falkingham P.L. (2019). Repeated evolution of drag reduction at the air-water interface in diving kingfishers. *Journal of the royal society interface*, 16(154), Article 20190125. https://doi.org/10.1098/rsif.2019.0125

[4] El Salem A., Zhang G., Wang H., Salem H., Abdalla M., & Ghazy A. (2023). The effect of integrating a bio-inspired convex structure with a low-surface energy polymer on soil adhesion and friction. *Journal of Terramechanics*, 109, 93–100. https://doi.org/10.1016/j.jterra.2023.06.003

[5] Guan C.S., Fu J.J., Xu L., Jiang X.Z., Wang S.L., & Cui Z.C. (2022). Study on the reduction of soil adhesion and tillage force of bionic cutter teeth in secondary soil crushing. *Biosystems engineering*, 213, 133–147. https://doi.org/10.1016/j.biosystemseng.2021.11.018

[6] Lei C., Xie F., Wu F.C., & Yan Q. (2024). Research on bionic design of cylindrical milling cutter based on the curvilinear configuration of the rake face of beaver teeth. *International journal of advanced manufacturing technology*, 130(9-10), 4905–4917. https://doi.org/10.1007/s00170-024-12951-y

[7] Li B., Chen Y., & Chen J. (2016). Modeling of soil-claw interaction using the discrete element method (DEM). *Soil & Tillage research*, 158, 177–185. https://doi.org/10.1016/j.still.2015.12.010

[8] Li K., Nagy D., Keller T., & Tamás K. (2026). Evaluating the effects of earthworm tip geometry on burrowing forces using cone penetration analogues and GPU-based discrete element method (DEM) simulations. Soil & Tillage research, 259, 16, Article 107069. https://doi.org/10.1016/j.still.2026.107069

[9] Lin S.B., Sun H.Y., Yan G.E., Que K.X., Xu S.J., Tang Z., Wang G.Q., & Li J.L. (2025). Structural Design and Analysis of Bionic Shovel Based on the Geometry of Mole Cricket Forefoot. *Agriculture*-Basel, 15(8), Article 854. https://doi.org/10.3390/agriculture15080854

[10] Liu G., Yao J., Chen Z., Han X., & Zou M. (2023). Mesoscopic analysis of drag reduction performance of bionic furrow opener based on the discrete element method. *Plos One*, 18(11), e0293750. https://doi.org/10.1371/journal.pone.0293750

[11] Liu G.M., Han X.K., Wang Z.Y., Wang K., Zhang Z.S., & Duan Z.A. (2024). Viscosity Reduction and Drag Reduction Performance Analysis of Bionic Excavator Buckets Based on Discrete Element Method. *Biomimetics*, 9(11), Article 686. https://doi.org/10.3390/biomimetics9110686

[12] Liu S.H., Weng S.J., Liao Y.L., & Zhu D.Y. (2014). Structural bionic design for digging shovel of cassava harvester considering soil mechanics. *Applied bionics and biomechanics*, 11(1-2), 1–11. https://doi.org/10.3233/ABB-140089

[13] Niu J.P., Luo T.Y., Xie J.Q., Cai H.X., Zhou Z.K., Chen J., & Zhang S. (2022). Simulation and experimental study on drag reduction and anti-adhesion of subsoiler with bionic surface. *International journal of agricultural and biological engineering*, 15(4), 57–64. https://doi.org/10.25165/j.ijabe.20221504.6531

[14] Obour P.B., Keller T., Jensen J.L., Edwards G., Lamande M., Watts C.W., Sorensen C.G., & Munkholm L.J. (2019). Soil water contents for tillage: A comparison of approaches and consequences for the number of workable days. *Soil and Tillage Research*, 195. https://doi.org/10.1016/j.still.2019.104384

[15] Sun J.F., Chen H.M., Wang Z.M., Ou Z.W., Yang Z., Liu Z., & Duan J.L. (2020). Study on plowing performance of EDEM low-resistance animal bionic device based on red soil. *Soil and Tillage Research*, 196, Article 104336. https://doi.org/10.1016/j.still.2019.104336

[16] Tong J., Sun J.Y., Chen D.H., & Zhang S.J. (2005). Geometrical features and wettability of dung beetles and potential biomimetic engineering applications in tillage implements. *Soil and Tillage Research*, 80(1-2), 1–12. https://doi.org/10.1016/j.still.2003.12.012

[17] Wang H.H., Li Y.M., Wu Y., Ji K.Z., & Liu Y.B. (2025). Design and experimental study of bionic digging shovel based on vole's front middle toe. *Journal of agricultural engineering*, 56(4), Article 1831. https://doi.org/10.4081/jae.2025.1831

[18] Wu B.G., Zhang R.Z., Hou P.F., Tong J., Zhou D.Y., Yu H.Y., Zhang Q., Zhang J.S., & Xin Y.L. (2021). Bionic Nonsmooth Drag Reduction Mathematical Model Construction and Subsoiling Verification. *Applied bionics and biomechanics*, 2021, Article 5113453. https://doi.org/10.1155/2021/5113453

[19] Xu Z.H., Qi H.Y., Gao P., Wang S., Liu X.T., & Ma Y.H. (2024). Biomimetic Design of Soil-Engaging Components: A Review. *Biomimetics*, 9(6), Article 358. https://doi.org/10.3390/biomimetics9060358

[20] Zhang F.B., Luo Z.T., Zheng E.L., Han L., Qian J., Yao H.P., Shi Y.Y., & Wang X.C. (2025). Imitating pangolin scale structure for reducing adhesion and resistance of rotary tillage in wet-adhesive soil. *Soil and Tillage Research*, 245, Article 106306. https://doi.org/10.1016/j.still.2024.106306

[21] Zhang R., Li G.Y., Ma S.S., Pang H., Ren L., Zhang H., & Su B. (2021). Frictional performance of ostrich (Struthio camelus) foot sole on sand in all directions. *Biomechanics and modeling in mechanobiology*, 20(2), 671–681. https://doi.org/10.1007/s10237-020-01409-1

[22] Zhang X.Y., Wang X., Wang W., Xu R.X., Li C.L., & Zhang F. (2021). Effects of Personality Traits on the Food-Scratching Behaviour and Food Intake of Japanese Quail (Coturnix japonica). *Animals*, 11(12), Article 3423. https://doi.org/10.3390/ani11123423